UCLA
UCLA Previously Published Works

Title
Spectroscopic and X-ray diffraction investigation of the behavior of hanksite and tychite at high pressures, and a model for the compressibility of sulfate minerals

Authors
Palaich, Sarah EM
Manning, Craig E
Schauble, Edwin
et al.

Spectroscopic and X-ray diffraction investigation of the behavior of hanksite and tychite at high pressures, and a model for the compressibility of sulfate minerals

Sarah E.M. Palaich,* Craig E. Manning, Edwin Schauble, and Abby Kavner

Department of Earth and Space Sciences, University of California, Los Angeles, California 90095, U.S.A.

Abstract

The rare evaporite minerals hanksite, $Na_{22}K(SO_4)_9(CO_3)_2Cl$, and tychite, $Na_6Mg_2(CO_3)_4(SO_4)$, are excellent case studies for the high-pressure behavior of ionic groups since their structures combine ionic complexity and high symmetry (hexagonal $P6_3/m$ and cubic $Fd3$, respectively). Here we investigate the structure and compressibility of hanksite up to 20 GPa in the diamond-anvil cell using Raman spectroscopy and X-ray diffraction and of tychite up to 17 GPa in the diamond cell using X-ray diffraction and first-principles modeling. At ambient pressure, the Raman spectrum of hanksite has a single sulfate ν_1 frequency at 992 cm^{-1} with a lower-frequency shoulder. As pressure is increased, this mode splits into two distinct peaks, which arise from two distinct local environments for the sulfate tetrahedra within the hanksite structure. Below 10 GPa, the mode Grüneisen parameter of the dominant sulfate ν_1 frequency is 0.27(1); the mode Grüneisen parameter of the lower frequency shoulder is 0.199(7). X-ray diffraction data of hanksite indicate a 5% volume drop between 8–10 GPa with no apparent change of symmetry. A Birch-Murnaghan fit to the data below 8 GPa yields an isothermal bulk modulus of 66(1) GPa for hanksite and 85(1) GPa for tychite, with K' fixed at 4.

Keywords: High pressure, X-ray diffraction, Raman spectroscopy, evaporite salt, sulfate, carbonate

Introduction

Hanksite, $Na_{22}K(SO_4)_9(CO_3)_2Cl$, is a rare evaporite mineral most commonly found in the Quaternary lacustrine evaporite deposit at Searles Lake, San Bernardino County, California (Pratt 1897; Eugster and Smith 1965). Some of the sulfate-rich deposits observed on Mars (Wang et al. 2006; Steiger et al. 2011) have been proposed to be evaporite beds caused by deposition from arid saline lakes, similar to Searles Lake (Barbieri and Stivaletta 2011). Hydrated salts with similar ionic constituents are thought to dominate the mantles of the icy moons of the outer planets (Chio et al. 2004; Brand et al. 2010). Ganymede's outer icy mantle may contain 15–20 wt% sulfates and studies predict a sulfate-dominated layer at the base of an 800 km icy mantle (Nakamura and Ohtani 2011). Therefore, understanding the behavior of sulfate-rich minerals can provide insights into the chemical and physical properties of the surfaces and interiors of Solar System bodies.

Only a handful of minerals including hanksite and tychite contain both sulfate and carbonate groups; hanksite is unique in that it contains (Na,K)Cl ionic groups as well. This ionic complexity combined with hanksite's hexagonal symmetry make it an ideal mineralogical model for the behavior of complex ionic systems under pressure. Figure 1 illustrates the hanksite unit cell from the *a*-axis, *c*-axis, and N(111) perspectives. Hanksite has cell parameters $a = 10.494(1)$ and $c = 21.190(3)$ Å, with a volume of 2020.8(8) Å^3, a Z of 2, and 154 atoms in the unit cell. The hexagonal symmetry belongs to space group $P6_3/m$ (Kato and Saalfeld 1972; Araki and Zoltai 1973). Carbonate triangles lie in a plane perpendicular to the *c*-axis. Chains of sodium and potassium octahedra run parallel to the *c*-axis and are connected by the sulfate tetrahedra and carbonate triangles (Araki and Zoltai

1973). The S-O bond lengths range from 1.463–1.485 Å, which is within the normal range of a non-distorted sulfate tetrahedron. As can be seen in Figure 1, the sulfate tetrahedra occupy two distinct bonding environments. Some sulfate groups are bonded to sodium polyhedra that include both oxygen and chlorine atoms while others are bonded only to regular sodium and/or potassium polyhedra including only oxygen atoms.

The high-pressure behavior of the sulfates gypsum and anhydrite have been studied both theoretically (Gracia et al. 2012) and experimentally via X-ray diffraction and IR/Raman spectroscopy methods (Bradbury and Williams 2009; Comodi et al. 2008; Ma et al. 2007; Knittle et al. 2001; Chen et al. 2001; Huang et al. 2000). In addition, much study has gone into $MgSO_4$, $BaSO_4$, various lithium sulfates, and sulfate salts (Lemos et al. 1991; Sakuntala and Arora 1999, 2000; Chen et al. 2009, 2010; Brand et al. 2010; Machon et al. 2010; Crichton et al. 2011; Jahn and Schmidt 2010; Zhang and Sekine 2007; Santamaría-Pérez et al. 2011; Antao 2012). Hydrated sulfates like gypsum undergo several structural changes below 10 GPa, while others like $BaSO_4$ exhibit few signs of transformation up to 20 GPa. The behavior of these compounds under pressure can be rationalized in terms of the local polyhedral behavior of the cations present in the structure, since SO_4 bond lengths and angles are expected to be relatively resistant to compression or distortion. Hanksite and tychite afford the opportunity to study this diverse behavior of sulfate under pressure in complex ionic compounds.

Experimental setup

The hanksite and tychite samples collected at Searles Lake were confirmed by X-ray diffraction. Powders were created by grinding samples in a mortar and pestle and were loaded into a 350 μm hole drilled in a precompressed steel gasket within a diamond-anvil cell (500 μm culets). No additional pressure medium was included due to the high solubility of hanksite and tychite in most fluids. Effects of a possibly non-hydrostatic sample environment are addressed in the discussion section. Small

crystals of ruby were placed in multiple locations in the cell for ruby fluorescence pressure determinations (Mao et al. 1986). For hanksite the reported pressure is the average and standard deviation of pressures measured by several different ruby fluorescence measurements obtained between each pressure step. Two sets of Raman spectroscopy experiments were performed on hanksite and one X-ray diffraction experiment was performed on hanksite followed by another X-ray diffraction experiment on tychite. Fresh samples were used for each experiment.

Raman spectra of hanksite were collected as a function of pressure and room temperature using a microscope-based confocal Raman system in the UCLA Mineral Physics Lab equipped with a 488 nm Ar+ laser, a 750 mm monochromator, a grating of 1800 grooves/mm and a resolution of 0.50 cm^{-1}/pixel (Hunt et al. 2011). The spectrometer was calibrated using a neon gas lamp before each experiment. In a first experiment, the pressure was increased in ~2 GPa steps to 16.60(6) GPa. Spectroscopic data were collected between 800–1300 cm^{-1}, encompassing the v_1 and v_3 internal modes of sulfate and the v_1 internal mode of carbonate. Data collection times ranged from 3–5 min with exposure time increasing with pressure. The cell was then left sitting for a week at high pressure. Upon decompression the signal to noise ratio was extremely poor and useful Raman signals could not be recovered below ~8 GPa. The cause of signal loss has not yet been determined. A second set of experiments examined the Raman spectra of hanksite under compression and subsequent decompression over the course of several hours. In this case, immediate decompression led to no signal loss.

In addition to the high-pressure Raman spectra, ambient-pressure spectra were collected on several additional species including laboratory-grade MgSO$_4$ powder, single-crystal gypsum, single-crystal hanksite, and single-crystal tychite. For these measurements data was collected from 200 to 1300 cm^{-1} and in the area of the O-H bonds ~3400 cm^{-1}. During the measurements of hanksite, different crystal orientations produced different frequencies depending on the laser polarization and the orientation of the crystal.

Angle-dispersive powder X-ray diffraction patterns at ambient temperature and high pressure were obtained at Beamline 12.2.2 at the Advanced Light Source at Lawrence Berkeley National Laboratory using a wavelength of 0.6199 Å. The image

detector distance was calibrated using a LaB$_6$ standard at the sample position. For hanksite, 15 pressure steps of ~1 GPa were taken to reach a high pressure of 15(2) GPa and 12 measurements were taken during decompression. The experiment on tychite was taken to 17.2(8) GPa in pressure steps of ~2 GPa.

The Mar345 image plate exposures were processed using the software Fit2D (Hammersley 1996) to create a two-dimensional "caked" image (e.g., Fig. 2). In-house software (M. Armentrout, in preparation) was used to integrate the two-θ positions of each individual diffraction peak, yielding a best-fit d-spacing and error bar for each lattice plane. Best-fit lattice parameters were calculated using a weighted linear least squares fit to the collection of d-spacings at each pressure step, assuming hexagonal symmetry for hanksite and cubic symmetry for tychite (Tables 1 and 2). Values for d-spacings at each pressure step are tabulated in the supplementary materials section[1] (Supplemental Table 1). Unlike the X-ray pattern integration package in Fit2D, our approach allows for identification and resolution of close peaks and immediate awareness of spurious information in two-dimensional X-ray diffraction patterns.

In addition to the experimental X-ray diffraction and Raman spectroscopy, a model for the pressure dependence of tychite's volume was created using density functional theory, with the PBE Gradient corrected functional (Perdew et al. 1996). The software QUANTUM Espresso (Giannozzi et al. 2009) and ultrasoft pseudopotentials (Table 3) were used to optimize the primitive unit cell of tychite for a range of energy cutoffs from 40 to 80 Rydberg at a single electronic wave vector (½, ½, ½). At 816 eV (60 Rydberg), the calculations were converged with respect to unit-cell volume (0.05%) and with respect to energy (0.00019 eV/atom). The calculated primitive unit-cell volume of 695.57 Å^3 is 3.4% larger than the value of 671.96 Å^3 from Schmidt et al. (2006). This is typical and expected for a PBE model

---

[1] Deposit item AM-13-802, Deposit tables and figures. Deposit items are available two ways: For a paper copy contact the Business Office of the Mineralogical Society of America (see inside front cover of recent issue) for price information. For an electronic copy visit the MSA web site at http://www.minsocam.org, go to the *American Mineralogist* Contents, find the table of contents for the specific volume/issue wanted, and then click on the deposit link there.
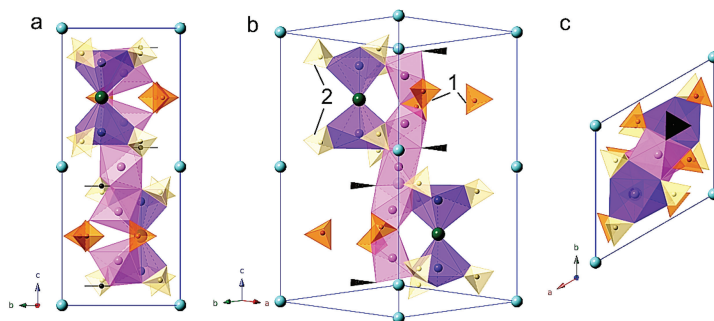

FIGURE 1. The hanksite unit cell from three perspectives. (**a**) View down *a*-axis, (**b**) view down N(111), and (**c**) view down *c*-axis. Potassium atoms line the unit-cell borders forming chains of potassium octahedra parallel to the *c*-axis. The two different types of sodium octahedra are shown in light (regular) and dark (coordinated with Cl). Carbonate triangles sit parallel to the *a*-axis in line with the chlorine atoms. Examples of the two distinct sulfate groups are labeled 1 (dark tetrahedra) and 2 (light tetrahedra). Dark sulfate groups are only bonded to regular sodium and potassium octahedra, while light groups are bonded to distorted octahedra. (Color online.)
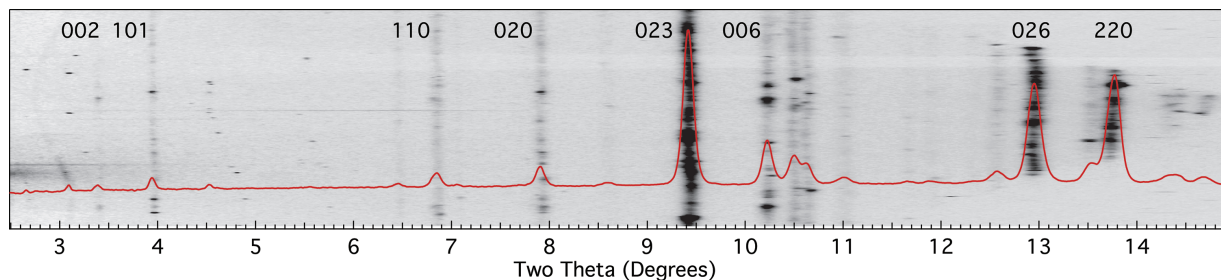

FIGURE 2. Diffraction pattern of hanksite at 2.8 GPa. Data integrated by Fit2D overlies the caked image. Selected lattice planes are labeled at the top left of their band. Note that instances of multiple peaks are much easier to identify in the "caked" image. (Color online.)

of an anhydrous crystal. Calculations were performed at several unit-cell volumes, corresponding to a maximum pressure of 18.5 GPa.

RESULTS AND DISCUSSION

Raman spectroscopy

Figure 3 depicts the polarized Raman spectra of hanksite at ambient pressure and temperature. The most intense Raman vibration corresponds to the SO_4 ν_1 symmetric stretch, which dominates the ambient- and high-pressure spectra. Our measured hanksite spectrum exhibits seventeen Raman peaks, including 15 sulfate internal modes and 2 carbonate internal modes, compared with the 35 Raman-active modes predicted by our factor-group analysis ($7A_g + 8E_{2g}^2 + 6E_{1g}^1 + 8E_{2g}^1 + 6E_{1g}^2$).

Table 4 gives a full listing of our ambient-pressure experimental hanksite and tychite frequencies in comparison to previous sulfate vibrational data. The values of the sulfate internal modes depend on the local bonding structure. The aqueous SO_4 ion ν_1 is

980 cm^{-1} (Nakamoto 1997), but in a contact ion pair with $MgSO_4$ the frequency shifts to 988 cm^{-1} (Jahn and Schmidt 2010). Comparing $BaSO_4$ and $SrSO_4$ illustrates the impact of bond length on sulfate modes. Sulfate ν_1 of $SrSO_4$ has a higher frequency than ν_1 of $BaSO_4$ because the shorter bond length between strontium and oxygen has a higher bond strength (Chen et al. 2009). Further examples of shifts in ν_1 due to differing local polyhedral environments can be found in $MgSO_4$ hydrates studied by Wang et al. (2006) and studies of lithium and sodium sulfates (Matsumoto et al. 2009).

Figure 4 shows the Raman spectra as a function of pressure. Above 1.4(1) GPa, the 992 cm^{-1} sulfate symmetric stretching mode (ν_1) becomes two distinct modes, each with a different pressure dependence. The carbonate ν_1 mode loses intensity above ~10 GPa and reappears upon decompression. A plot of the

TABLE 1. Hanksite hexagonal lattice parameters

Pressure (GPa)	a	c
0	10.487(1)	21.232(5)
2.8(2)	10.359(2)	20.859(6)
3.7(2)	10.347(3)	20.809(11)
4.6(5)	10.284(4)	20.662(14)
6.0(6)	10.257(3)	20.571(11)
6.7(7)	10.232(3)	20.507(12)
7.1(7)	10.213(3)	20.459(10)
8.1(8)	10.178(3)	20.364(10)
9.0(9)	10.135(4)	20.215(12)
9.8(8)	10.066(4)	20.048(10)
10.4(7)	10.010(4)	19.923(12)
11.5(15)	9.988(5)	19.833(13)
12.4(15)	9.957(4)	19.756(11)
13.0(15)	9.934(5)	19.695(12)
14(2)	9.910(4)	19.677(11)
15(2)	9.919(5)	19.713(13)

Note: Parameters *a* and *c* from ambient to 15(2) GPa.

TABLE 2. Tychite cubic lattice parameter

Pressure (GPa)	a
0.41(6)	13.886(2)
1.92(6)	13.833(4)
3.9(1)	13.715(5)
5.11(6)	13.656(4)
7.08(3)	13.573(4)
8.77(3)	13.519(3)
10.61(8)	13.450(4)
12.3(2)	13.423(8)

Notes: Parameter *a* from 0.41(6) to 12.3(2) GPa. Diffraction patterns beyond this pressure have a different symmetry.

TABLE 3. Pseudopotentials used in the first-principles tychite model

Carbon	C.pbe-rrkjus.UPF[1]
Magnesium	Mg_2-5-07.ncpp[2]
Oxygen	O.pbe-rrkjus.UPF[1]
Sodium	Na.pbe-sp-van_ak.UPF[1]
Sulfur	S.pbe-van_ak.UPF[1]

[1] From http://www.quantum-espresso.org.
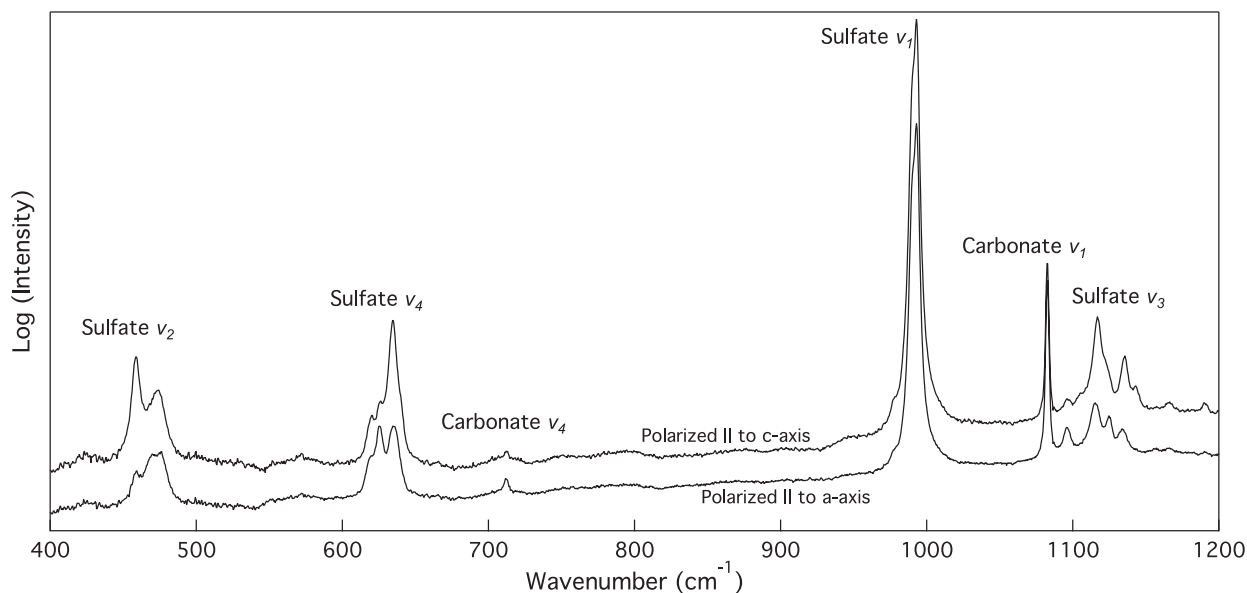[2] Moynier et al. (2011).

FIGURE 3. Ambient-pressure polarized Raman spectra of hanksite. The ν_1 mode of the sulfate tetrahedra dominates the pattern at 992 cm^{-1}. The majority of the modes occur in the ν_3 antisymmetric stretch region between 1096 and 1190 cm^{-1}. Crystal orientation affects the presence and intensity of both carbonate and sulfate modes. In the upper pattern, the laser is polarized approximately parallel to the *c* axis, while in the lower pattern it is polarized approximately parallel to the *a* axis.

TABLE 4. Raman frequencies of various sulfate minerals

Mode	Hanksite[1]	Tychite[1]	Tychite[2]	MgSO4[1]	MgSO4[3]	Gypsum[1]	Gypsum[4]	SO4ion[5]	Anhydrite[6]	Barite[7]	SrSO4[8]	LiCsSO4[9]
Sulfate v_1	992.8	970	967	983.8	1022.8	1009	1002	983	1016	988	1001	1016
	995			1021.8	1052		1008					
	1049			1051								
Sulfate v_2	459		493.8		451	419	412	450	416	451	50 8/9	448.1
	470				475	497	492		498	461		461
	474				499							
Sulfate v_3	1096	1103	1136.6	1136	1136	1142	1120	1105	1111	1142	1055	1108
	1117	1137			1220		1137		1128	1169	1094	1110.5
	1124						1150		1159		1111	1125
	1135										1158	1158.5
	1142										1189	1198
	1156											
	1166											
	1190											
Sulfate v_4	620		629		608	621	605	611	608	617	622	620
	625				681		621		627	646	639	623
	634				697		670		674		656	650
							672					

Notes: The tychite and MgSO4 studies in this work did not include the lower-frequency range of modes v_2 and v_4. [1]Raman data from this study; [2]Schmidt et al. (2006); [3]Wang et al. (2006); [4]Knittle et al. (2001); [5]Nakamoto (1997); [6]Zhang and Sekine (2007); [7]Lee et al. (2003); [8]Chen et al. (2010); [9]Lemos et al. (1991).

sulfate v_1 and v_3 and carbonate v_1 modes as a function of pressure (Fig. 5) shows the pressure-reversibility and the reproducibility in experiments. The pressure dependence of these modes and their mode Grüneisen parameters are listed in Table 5.

Huang et al. (2000) and Comodi et al. (2008) observe a splitting in the sulfate v_1 mode in gypsum at 4–6 GPa. They interpret the splitting as distortion of the sulfate tetrahedra due to changing water molecule geometry. Knittle et al. (2001) also observe the split at 4–6 GPa and conclude that the split is due to pressure-induced Fermi resonance with the overtone of the v_2 symmetric bending vibration. In our case, no such overtones are readily apparent in our hanksite spectra, supporting the idea that the two distinct v_1 peaks arise from the two distinct geometries of sulfate tetrahedra as indicated in Figure 1.

X-ray diffraction

At ambient conditions the measured unit-cell parameters of hanksite were $a = 10.494(1)$ Å and $c = 21.190(3)$ Å, with a unit-cell volume of 2020.8(8) Å^3, in good agreement with previously published values by Kato and Saalfeld (1972) of $a = 10.490(1)$ Å and $c = 21.240(1)$ Å and Araki and Zoltai (1973) of $a = 10.465(21)$ Å and $c = 21.191(43)$ Å. Figure 6 plots normalized volume as a function of pressure for hanksite and tychite diffraction data. For hanksite, the X-ray diffraction patterns are consistent with a hexagonal symmetry for all pressure steps. Integrated diffraction patterns are included in Supplementary Figure 1 and lattice data are tabulated in Supplementary Table 1[1]. A Birch-Murnaghan fit to the volume compression data between 0 and 8 GPa yields an isothermal bulk modulus of 66(1) GPa (with $K' = dK_{0,T}/dP$ fixed at 4). A Birch-Murnaghan fit of the unit-cell parameters a and c with respect to pressure yield effective bulk moduli of 76(2) GPa for a and 50(2) GPa for c. This is consistent with the orientation of the carbonate triangles parallel to the a axis reducing the a axis compressibility and the large amount of compressible octahedra stacked along the c axis.

Tychite [Na$_6$Mg$_2$(CO$_3$)$_4$(SO$_4$)] has a cubic (*Fd*3) structure with similar polyhedral components (Schmidt et al. 2006). X-ray diffraction under pressure shows this structure is stable up to 10.61(8) GPa. A Birch-Murnaghan fit to the tychite high-pressure data in this range gives an initial volume of 2693(2)
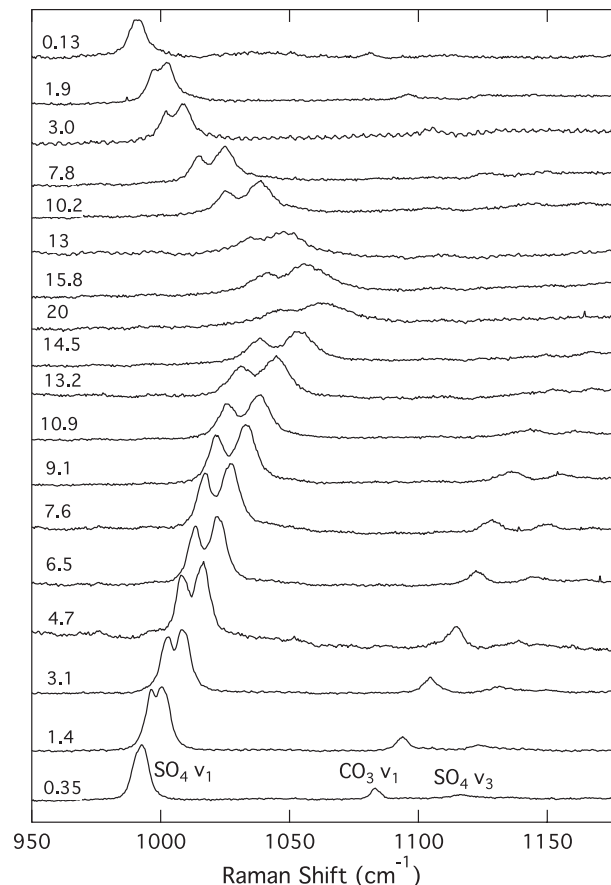

FIGURE 4. Raman spectra of hanksite as a function of pressure. Pressure in GPa of each spectrum is indicated to the top left of each pattern. Separation of the two v_1 modes occurs immediately. Upon decompression, the modes return to their original frequencies and merge back together.

Å^3 and an isothermal bulk modulus of 85(1) GPa (with K' fixed at 4). This unit-cell volume compares well with 2687.82(7) Å^3 found by Schmidt et al. (2006). The tychite experiment yields a bulk modulus smaller than the first-principles model of tychite
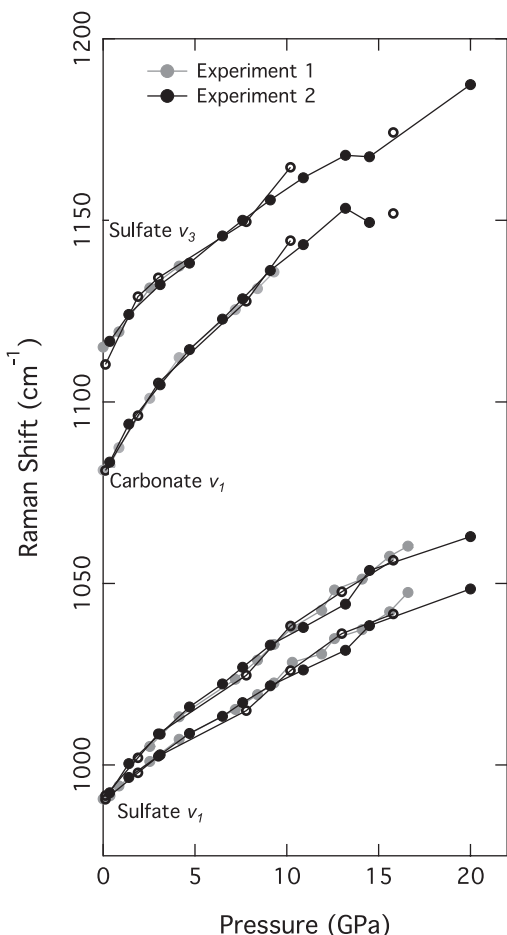
FIGURE 5. Raman shift vs. pressure for both hanksite experiments. First hanksite experiment (gray circles), second hanksite experiment (dark gray circles), and second hanksite experiment decompression (open circles) are shown for three modes.

TABLE 5. Hanksite sulfate v_1 and v_3 and carbonate v_1 pressure dependence and mode Grüneisen parameters

Mode	Pressure dependence (cm^{-1}/GPa)	Mode Grüneisen parameter
Sulfate v_1	4.0(2)	0.27(1)
Sulfate v_1 Shoulder	3.0(1)	0.199(7)
Carbonate v_1	5.3(2)	0.32(1)
Sulfate v_3	3.9(2)	0.23(1)

Notes: Mode Grüneisen parameters calculated from $\gamma_i = (K_{0,T}/v_0)(dv_i/dP)_T$ (Knittle et al. 2001) using the bulk modulus 66(1) GPa determined in the X-ray diffraction experiment. Mode Grüneisen parameters compare to sulfate v_1 parameter of 0.21(2) in gypsum and a sulfate v_1 parameter of 0.6(2) in pressurized anhydrite (Knittle et al. 2001; Bradbury and Williams 2009).

and only up to 8 GPa. Although we lack direct data on supported differential stress for this experiment, we can provide an estimate of our systematic bias on our measured bulk modulus by assuming that hanksite and tychite have similar strengths as those reported for NaCl (Meade and Jeanloz 1988). At 8 GPa, corresponding to the maximum pressure used to determine compressibility in the current study, NaCl supports a differential stress of ~0.25 GPa. If we assume that hanksite and tychite support a differential stress of ~0.5 GPa at 8 GPa, we calculate that our determined bulk moduli may be overestimated by ~6%; e.g., 62 GPa for hanksite rather than 66 GPa. We acknowledge that lack of hydrostaticity may cause our measured bulk moduli to be systematically biased higher, but argue that the effect is small (~6% maximum) and does not affect any of the main conclusions of our study.

Sulfate systematics

Figure 7 shows V/V_0 as a function of pressure for hanksite, tychite, and several additional sulfate minerals. At pressures below ~8 GPa, hanksite's compressibility is similar to previous measurements of BaSO$_4$ compressibility (Lee et al. 2003;

volume as a function of pressure, which yields $K_{0,T} = 132(1)$ GPa (with K' fixed at 4). In the diffraction experiments we observe evidence of a transition in the tychite unit-cell structure by 12–15 GPa. Near 12 GPa, the (111) lattice plane disappears, calling into question our assumption of $Fd3$ cubic symmetry. The new structure has not yet been identified. Tychite integrated diffraction patterns and lattice data are given in Supplementary Table 2[1] and Supplementary Figure 2[1].

Effects of non-hydrostaticity

Our sample, which could not be loaded with a liquid pressure medium due to its high solubility, may be subjected to a non-hydrostatic sample chamber. Generally these non-hydrostatic effects—which result in larger-than hydrostatic measured X-ray lattice parameters in the X-ray and diamond-cell geometry employed in these studies—arise when a sample is able to support a great deal of differential stress. Figures depicting the pressure evolution of hanksite and tychite diffraction patterns are provided in Supplemental Figures 1[1] and 2[1]. By 9–10 GPa, notable broadening of peaks is seen in both hanksite and tychite patterns. Equation-of-state fits to the data were conducted below these pressures
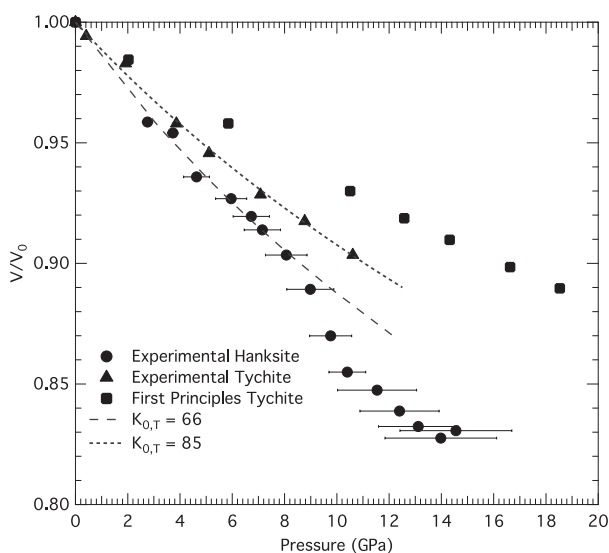

FIGURE 6. Plot of normalized volume as a function of pressure for hanksite (experimental: filled circle) and tychite (experimental: filled triangle, model: filled box) from X-ray diffraction data and first-principles model. Error bars on hanksite pressure represent the standard deviation of pressures measured in the DAC. Birch-Murnaghan fits to the experimental data are shown as dotted lines [hanksite $K_{0,T} = 66(1)$ GPa; tychite $K_{0,T} = 85(1)$ GPa].

Crichton et al. 2011). Beginning at 8 GPa and ending at 10 GPa the hanksite data show a volume drop of 5%, but with no apparent change of symmetry to indicate a first-order phase transition. A similar trend was determined from the ab initio calculations for mirabilite ($Na_2SO_4 \cdot 10H_2O$), which undergoes a volume drop of 20% between 7 and 10 GPa (Brand et al. 2010). In contrast, tychite is slightly less compressible than hanksite and barite and its pressure-volume relationship is smooth until its structural change near 12 GPa. The first-principles model of tychite is much less
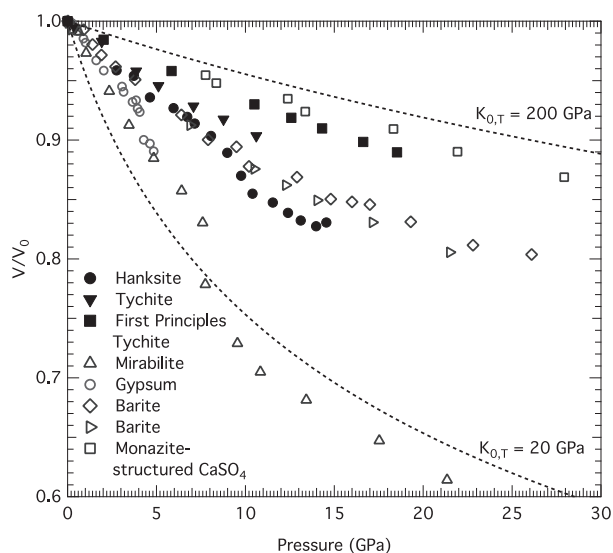
FIGURE 7. Plot of normalized volume as a function of pressure for various sulfate minerals. Birch-Murnaghan P-V curves are shown for $K_{0,T} = 200$ GPa and $K_{0,T} = 20$ GPa (dotted lines, K' fixed at 4). Sulfate mineral data from Lee et al. 2003 (open diamond); Comodi et al. 2008 (open circle); Bradbury and Williams 2009 (open box); Brand et al. 2010 (open triangle); and Crichton et al. 2011 (open right-pointing triangle). For clarity in seeing trends, we have omitted error bars from this plot.
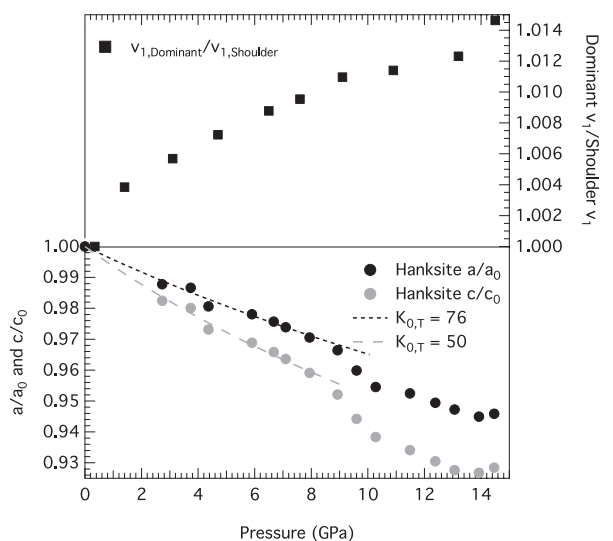

FIGURE 8. Ratio of sulfate v_1 modes and normalized compressibilities of a and c axes. Fits to the Birch-Murnaghan equation of state from below 8 GPa are shown for both a and c. Note the discontinuity in both the Raman and X-ray data near 10 GPa.

compressible and is most akin to the monazite-structured $CaSO_4$ (Bradbury and Williams 2009).

Data from tychite, gypsum, $SrSO_4$, and $LiCsSO_4$ (Knittle et al. 2001; Comodi et al. 2008; Chen et al. 2010; Shashikala et al. 1993) all exhibit strong evidence for first-order phase transitions. Lattice planes and symmetries change and the sulfate modes split near phase transitions. Hanksite shows no change in symmetry; diffraction peaks neither appear nor disappear during the volume shift between 8 and 10 GPa. Hanksite's behavior is closer to that of $SrSO_4$ and $SnSO_4$. Raman studies of $SrSO_4$ by Chen et al. (2010) found a discontinuity of the v_1 mode with respect to pressure at 10 GPa interpreted as a second-order phase transition. The study of $SnSO_4$ by Hinrichsen et al. (2008) found a similar transition. Each of these transitions was isostructural and caused by the reordering and/or distortion of the surrounding polyhedra affecting the less compressible SO_4 groups.

Figure 8 compares the compressibility of the a and c axes of the hanksite unit cell to the ratio of the two v_1 modes above 1.4(1) GPa. All of these parameters exhibit a discontinuity in slope near 10 GPa. The c-axis is more compressible than the a-axis, but they both experience a drop in the same pressure range that the ratio of the v_1 modes appear to flatten. The flattening of the ratio of the v_1 modes corresponds to the slight kink seen in the Raman patterns (Fig. 5). These trends indicate a pressure-induced change in the local cation geometry surrounding the sulfate groups that does not affect the overall hexagonal symmetry.

Figure 7 demonstrates the wide range of compressibilities for sulfate minerals. We hypothesize that the elastic properties of sulfates are not controlled by the mechanical structure of the major functional SO_4 unit or unit-cell properties, but rather by the local environment of the sulfate groups within a mineral structure.
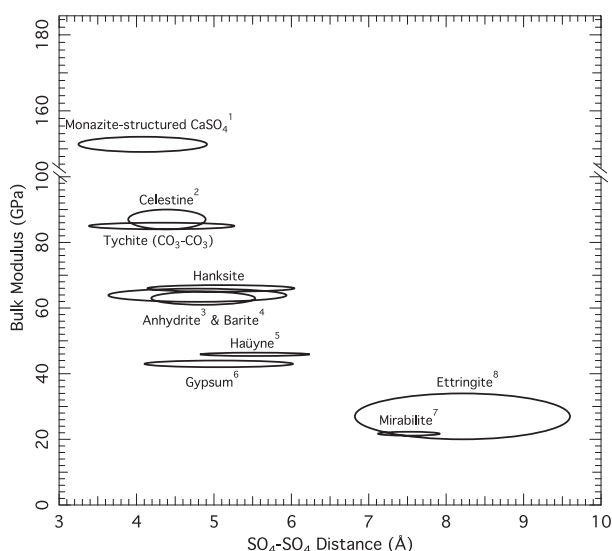

FIGURE 9. Correlation between isothermal bulk modulus and average SO_4-SO_4 distance in select minerals. Ellipses encompass standard deviation of SO_4-SO_4 distance in each mineral and the error in the isothermal bulk modulus calculation. Bulk modulus data from [1]Bradbury and Williams (2009); [2]Chen et al. (2010); [3]Gracia et al. (2012); [4]Crichton et al. (2011); [5]Fan et al. (2011); [6]Comodi et al. (2008); [7]Brand et al. (2010); and [8]Clark et al. (2008).

To test this hypothesis, we examine the relationship between the average distance between sulfate groups (or other incompressible polyhedra) and the isothermal bulk modulus for several sulfate-bearing minerals (Fig. 9). Minerals with large distances (>7 Å) between sulfate groups and no other incompressible polyhedra have low bulk moduli (ettringite and mirabilite) (Brand et al. 2010; Clark et al. 2008). As the distance between the sulfate groups decreases, the bulk modulus of the mineral increases exponentially. In tychite, the sulfate tetrahedra are far away from each other (~6 Å) compared to the carbonate triangles (~4.3 Å), so the carbonate groups are the important correlation factor. An estimate of the expected bulk modulus for a sulfate mineral can be achieved from this correlation given an idea of the distance between sulfate polyhedra.

REFERENCES CITED

Antao, S.M. (2012) Structural trends for celestite (SrSO$_4$), anglesite (PbSO$_4$), and barite (BaSO$_4$): Confirmation of expected variations within the SO$_4$ groups. American Mineralogist, 97, 661–665.

Araki, T., and Zoltai, T. (1973) The crystal structure of hanksite. American Mineralogist, 58, 799–801.

Barbieri, R., and Stivaletta, N. (2011) Continental evaporites and the search for evidence of life on Mars. Geological Journal, 46, 513–524.

Bradbury, S.E., and Williams, Q. (2009) X-ray diffraction and infrared spectroscopy of monazite-structured CaSO$_4$ at high pressures. Implications for shocked anhydrite. Journal of Physics and Chemistry of Solids, 70, 134–141.

Brand, H.E.A., Fortes, A.D., Wood, I.G., and Vočadlo, L. (2010) Equation of state and pressure-induced structural changes in mirabilite (Na$_2$SO$_4$·10H$_2$O) determined from ab initio density functional theory calculations. Physics and Chemistry of Minerals, 37, 5, 265–282.

Chen, C.-C., Liu, L.-G., Lin, C.-C., and Yang, Y.-J. (2001) High-pressure phase transformation in CaSO$_4$. Journal of Physics and Chemistry of Solids, 62, 1293–1298.

Chen, Y.-H., Huang, E., and Yu, S.-C. (2009) High-pressure Raman study on the BaSO$_4$-SrSO$_4$ series. Solid State Communications, 149, 2050–2052.

Chen, Y.-H., Yu, S.-C., Huang, E., and Lee, P.-L. (2010) Raman spectroscopy and X-ray diffraction studies on celestite. Physica B: Physics of Condensed Matter, 405, 4386–4388.

Chio, C.H., Sharma, S.K., and Muenow, D.W. (2004) Micro-Raman studies of gypsum in the temperature range between 9 K and 373 K. American Mineralogist, 89, 390–395.

Clark, S.M., Colas, B., Kunz, M., Speziale, S., and Monteiro, P.J.M. (2008) Effect of pressure on the crystal structure of ettringite. Cement and Concrete Research, 38, 1, 19–26.

Comodi, P., Nazzareni, S., Zanazzi, P.F., and Speziale, S. (2008) High-pressure behavior of gypsum: A single-crystal X-ray study. American Mineralogist, 93, 1530–1537.

Crichton, W.A., Merlini, M., Hanfland, M., and Muller, H. (2011) The crystal structure of barite, BaSO$_4$, at high pressure. American Mineralogist, 96, 364–367.

Eugster, H.P., and Smith, G.I. (1965) Mineral equilibria in the Searles Lake evaporites, California. Journal of Petrology, 6, 473–522.

Fan, D., Wei, S., Zhou, W., Liu, J., Li, Y., and Xie, H. (2011) Synchrotron X-ray diffraction study of haüyne at high pressure. Physica B: Physics of Condensed Matter, 406, 4404–4406.

Giannozzi, P., Baroni, S., Bonini, N., Calandra, M., Car, R., Cavazzoni, C., Ceresoli, D., Chiarotti, G., Cococcioni, L., Dabo, I., and others. (2009) QUANTUM ESPRESSO: a modular and open-source software project for quantum simulations of materials. Journal of Physics: Condensed Matter, 21, 395502.

Gracia, L., Beltrán, A., Errandonea, D., and Andrés, J. (2012) CaSO$_4$ and its pressure-induced phase transitions: a density functional theory study. Inorganic Chemistry, 51, 1751–1759.

Hammersley, A.P., Svensson, S.O., Hanfland, M., Fitch, A.N., and Hausermann, D.

(1996) Two-dimensional detector software: From real detector to idealised image or two-theta scan. High Pressure Research, 14, 235–248.

Hinrichsen, B., Dinnebier, R.E., Liu, H., and Jansen, M. (2008) The high pressure crystal structures of tin sulphate: a case study for maximal information recovery from 2D powder diffraction data. Zeitschrift für Kristallographie, 223, 195–203.

Huang, E., Xu, J.-A., Lin, J.-F., and Hu, J.-Z. (2000) Pressure-induced phase transitions in gypsum. High Pressure Research, 17, 1, 57–75.

Hunt, J.D., Kavner, A., Schauble, E.A., Snyder, D., and Manning, C.E. (2011) Polymerization of aqueous silica in H$_2$O–K$_2$O solutions at 25–200 °C and 1 bar to 20 kbar. Chemical Geology, 283, 161–170.

Jahn, S., and Schmidt, C. (2010) Speciation in aqueous MgSO$_4$ fluids at high pressures and high temperatures from ab initio molecular dynamics and Raman spectroscopy. The Journal of Physical Chemistry B, 114, 15565–15572.

Kato, K., and Saalfeld, H. (1972) The Crystal Structure of Hanksite and its Relation to the K$_2$SO$_4$ I Structure Type. Acta Crystallographia, B28, 3614–3617.

Knittle, E., Phillips, W., and Williams, Q. (2001) An infrared and Raman spectroscopic study of gypsum at high pressures. Physics and Chemistry of Minerals, 28, 630–640.

Lee, P.-L., Huang, E., and Yu, S.-C. (2003) High-pressure Raman and X-ray studies of barite, BaSO$_4$. High Pressure Research, 23, 439–450.

Lemos, V., Silveira, E.S., Melo, F.E.A., Filho, J.M., and Pereira, J.R. (1991) Raman study of LiCsSO$_4$. Physica status solidi (b), 164, 577–585.

Ma, Y.M., Zhou, Q., He, Z., Li, F.F., Yang, K.F., Cui, Q.L., and Zou, G.T. (2007) High-pressure and high-temperature study of the phase transition in anhydrite. Journal of Physics: Condensed Matter, 19, 425221.

Machon, D., Pinheiro, C.B., Bouvier, P., Dmitriev, V.P., and Crichton, W.A. (2010) Absence of pressure-induced amorphization in LiKSO$_4$. Journal of Physics: Condensed Matter, 22, 315401.

Mao, H.-K., Xu, J.-A., and Bell, P.M. (1986) Calibration of the ruby pressure gauge to 800 kbar. Journal of Geophysical Research, 91, 4673–4676.

Matsumoto, Y., Harada, H., Yui, K., Uchida, H., Itatani, K., and Koda, S. (2009) Raman spectroscopic study of aqueous alkali sulfate solutions at high temperature and pressure to yield precipitation. The Journal of Supercritical Fluids, 49, 303–309.

Meade, C., and Jeanloz, R. (1988) Yield strength of the B1 and B2 phases of NaCl. Journal of Geophysical Research, 93 (B4), 3270–3274.

Moynier, F., Yin, Q.Z., and Schauble, E. (2011) Isotopic evidence of Cr partitioning into Earth's core. Science, 331, 1417–1420.

Nakamoto, K. (1997) Infrared and Raman Spectra of Inorganic and Coordination Compounds: Part A, 387 p. Wiley, New York.

Nakamura, R., and Ohtani, E. (2011) The high-pressure phase relation of the MgSO$_4$-H$_2$O system and its implication for the internal structure of Ganymede. Icarus, 211, 648–654.

Perdew, J.P., Burke, K., and Ernzerhof, M. (1996) Generalized gradient approximation made simple. Physical Review Letters, 77, 3865–3868.

Pratt, J.H. (1897) On Northupite: Pirssonite, a new mineral; Gaylussite and Hanksite from Borax Lake, San Bernadino County, California. American Journal of Science, 2, 123–135.

Sakuntala, T., and Arora, A.K. (1999) High-pressure phase transitions in Li$_2$SO$_4$-H$_2$O. Physica B: Physics of Condensed Matter, 279, 282–289.

——— (2000) Pressure induced phase transitions in LiNaSO$_4$. Journal of Physics and Chemistry of Solids, 61, 103–108.

Santamaría-Pérez, D., Gracia, L., Garbarino, G., Beltrán, A., Chuliá-Jordán, R., Gomis, O., Errandonea, D., Ferrer-Roca, C., Martínez-García, D., and Segura, A. (2011) High-pressure study of the behavior of mineral barite by X-ray diffraction. Physical Review B, 84, 054102.

Schmidt, G.R., Reynard, J., Yang, H., and Downs, R.T. (2006) Tychite, Na$_6$Mg$_2$(SO$_4$)(CO$_3$)$_4$: structure analysis and Raman spectroscopic data. Acta Crystallographica, E62, i207–i209.

Shashikala, M.N., Chandrabhas, N., Jayaram, K., Jayaraman, A., and Sood, A.K. (1993) Pressure-induced phase transitions in LiRbSO$_4$. Journal of Raman Spectroscopy, 24, 129–132.

Steiger, M., Linnow, K., Ehrhardt, D., and Rohde, M. (2011) Decomposition reactions of magnesium sulfate hydrates and phase equilibria in the MgSO$_4$, H$_2$O and Na+Mg$_2$+Cl, SO$_4$, H$_2$O systems with implications for Mars. Geochimica et Cosmochimica Acta, 75, 3600–3626.

Wang, A., Freeman, J.J., Jolliff, B.L., and Chou, I.-M. (2006) Sulfates on Mars: A systematic Raman spectroscopic study of hydration states of magnesium sulfates. Geochimica et Cosmochimica Acta, 70, 6118–6135.

Zhang, F., and Sekine, T. (2007) Impact-shock behavior of Mg- and Ca-sulfates and their hydrates. Geochimica et Cosmochimica Acta, 71, 4125–4133.